Urban noise footprint of a multicopter drone

B. Van Genechten [1], **K. Kucukcoskun** [1], **A. Zarri** [2], **C. Schram** [3]
[1] Siemens Digital Industries Software, Acoustic Simulation, Product Manager,
Interleuvenlaan 68, 3001 Leuven, Belgium
e-mail: **korcan.kucukcoskun@siemens.com**

[2] von Karman Institute for Fluid Dynamics, Env. and Applied Fluid Dynamics Dept., Post-Doctoral Fellow,
Waterloosesteenweg 72, B-1640 Sint-Genesius-Rode, Belgium

[3] von Karman Institute for Fluid Dynamics, Aeronautics and Aerospace Dept., Professor,
Waterloosesteenweg 72, B-1640 Sint-Genesius-Rode, Belgium

Abstract
This paper describes a simulation methodology aiming at a quick assessment of the noise footprint of a drone within an urban environment. The two key aspects of this problem are noise generation, on the one hand, mostly linked to the drone intrinsic aeroacoustics, and noise propagation on the other hand, which depends upon the reflections from the built environment. Concerning the difference in size between small flow scales around the drone and the large buildings, a simulation methodology is considered without resolving the flow scales around the buildings but still taking their effects into account in acoustic propagation. This can be achieved with a hybrid approach coupling flow solution with acoustic propagation using ray acoustics. In this study, the free-field tonal noise simulations of the drone are first successfully cross-validated by experimental data. The Leuven city center is used to illustrate the propagation process using the results of the first step combined with a ray acoustics solution.

1 Introduction

Professional drone services for package delivery, medical supplies, or other purposes are meant to become part of our landscape very soon. While societal acceptance will depend on many factors, noise ranks as one of the key issues. The typical noise pattern of such a drone consists of a combination of electric motor and propeller noise. The propeller noise contribution, considered flow-induced noise, includes both tonal and broadband components. The tonal part represents the periodic behavior during the rotation of the acoustic sources, whereas the broadband part appears due to random turbulent structures around the propeller profile. Psychoacoustic studies show that the tonal part of the propagation is perceived as a higher annoyance for humans [1]. Therefore this paper focuses on the tonal part of the flow-induced noise.

The tonal drone noise can be computed using several alternative methods. One can simulate the complete drone and urban environment in a single Computational Fluid Dynamics solution. However, this might be computationally demanding since the required flow field resolution around the source and buildings vary significantly. A very high-fidelity solution around the reflective building walls is not needed in practice since only their acoustic contribution is needed. Alternatively, in order to simplify the simulation models and shorten computation times, the aeroacoustic problem can be split into multiple smaller parts where each step considers a different part of the complete picture. In the current study, the latter approach is applied to obtain an optimal combination of computations efficiency and prediction accuracy.

This paper covers two main aspects, the simulation methodology development and its applications for urban footprint prediction, respectively. In the Methodology section, the noise source input to the urban propagation model is obtained by an end-to-end workflow. A quadcopter model and the flow field around it are first described following the work in the related reference [2]. Using the flow output of the finite-volume based

aerodynamic solutions as input in a Finite-Element based acoustic propagation solution, the exterior acoustic propagation is computed including the reflections from the quadcopter airframe. The obtained results are validated with experiments available in the literature. Subsequently, a numerical study is performed in order to best describe the quadcopter as a point source with directivity for the urban propagation problem. The Methodology section also describes the theory of urban propagation using acoustic ray-tracing technologies.

Finally, in the Applications section, the acoustic directivity source obtained from the quadcopter is placed in front of a model representation of the library building located in Ladeuzeplein, Leuven, Belgium. In this way, the scattering effects of the ground and the building on the acoustic propagation are accurately taken into account. The demonstrated workflow is validated against analytical solutions with image sources assuming simplified reflective surfaces of the same geometry. The acoustic field at the facade of the library building is computed with realistic reflection contributions. Typical diffraction effects around the corners of buildings are also presented for the microphones located on the side streets of the library. To better understand the noise transfer path from the drone to the the observer, the ray-tracing simulations provide highly detailed results such as echograms showing the ray paths and their arrival time at an observer waiting in front of the library building.

2 Methodology

The study in this article is based on the DJI Phantom 3 Advanced commercial quadcopter [3]. NASA Ames Research Center, USA, provided the simplified fuselage geometry used in the numerical simulations detailed below. The key simplification is that the camera has been omitted to reduce the additional computational complexity associated with its discretization. It does, however, feature the landing gear and the four supporting arms that are joined to a central body. The absence of solid pieces representing brushless motors simplifies things even further. Since the space between the propeller's center and the supporting strut is relatively small, it has no effect on the overall flow characteristics. A DJI 9450 propeller with an average chord of roughly $0.025\,\mathrm{m}$ and a rotor diameter of $D = 0.239\,\mathrm{m}$ was employed. By mirroring the CAD in the spanwise direction, the clockwise version is created. Four propellers were employed in this study, and their respective beginning locations are illustrated in Figure 1(a).

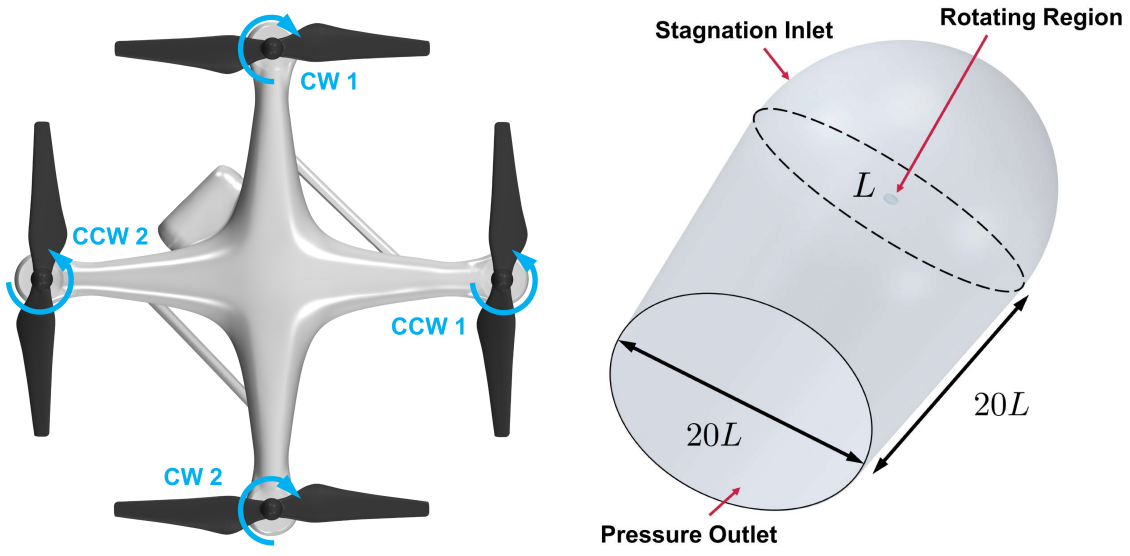

(a) (b)

Figure 1: (a) Four propellers' initial conditions: two turning clockwise (CW1 and CW2), two rotating counterclockwise (CCW1 and CCW2). (b) Bullet-shaped computational domain used for the URANS simulation.

2.1 Unsteady RANS simulation

The commercial solver Simcenter STAR-CCM+ Version 16.04 is used to compute the flow field using unsteady RANS (URANS). Figure 1(b) shows a bullet-shaped computational domain that is big enough to provide undisturbed conditions in locations far away from the moving parts. The domain has a width of $L = 1.1D$, which serves as the basis for the entire domain's creation. To model hovering, the boundary conditions were determined so as to have stagnation-inlet conditions everywhere except at the bullet-shaped domain's exit, where a pressure-outlet condition is applied. Within the rotating regions where the propellers are enclosed, a steady moving reference frame technique was explored to initiate the simulation (see, for example, related Reference [4]), then shifted to sliding-mesh for the unsteady solution. The propellers' rotating speed is set to $6000\ \mathrm{rpm}$, which corresponds to a rotational frequency of $\Omega = 100\,\mathrm{Hz}$. As a result, the simulation presents an incompressible subsonic flow regime with a Reynolds number in the turbulent transition range. In order to have $3°$ of rotating mesh displacement per time step Δt, $\Delta t = 8.3333 \cdot 10^{-5}\ \mathrm{s}$ is chosen. The k-ω SST turbulence model [5] and a second-order temporal discretization technique were used. The grid includes roughly $8 \cdot 10^6$ polyhedral cells, largely grouped around propellers and fuselage (see Figure 2(a) for a close-up picture of the mesh on the drone body and propeller). To attain a value of $y+ < 5$ everywhere,

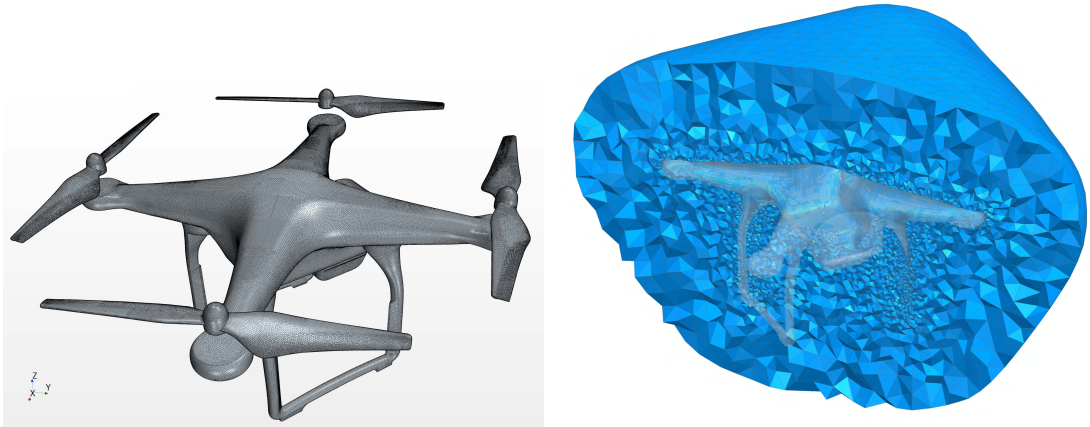

(a) (b)

Figure 2: (a) Polyhedral mesh generated on the drone's body. (b) Tetrahedral elements of the FEM mesh enclosing the drone's fuselage.

a thickness of $1\,\mathrm{mm}$ has been discretized by 20 prism layers. To validate the flow simulation results, the numerically obtained thrust value is compared against measurements carried out in the literature [6]. The simulation is considered validated as it presents a small relative difference below 1.4% with respect to the experiments.

2.2 Acoustic simulation using the Finite Element Method

The aerodynamic loads on the blade surfaces, computed using the URANS approach defined in Section 2.1, are used as input to an acoustic solver capable of computing discrete tones at BPF and harmonics. In particular, the commercial Simcenter Nastran [7] code is employed since it embeds a formulation in the frequency domain known as source formalism [8]. Here, the dipole source strengths are calculated by integrating the transient pressure field over acoustically compact blade segments. Three components of force per segment are analyzed in the radial, azimuthal, and axial directions. The solution reconstructs the rotating source as equivalent stationary components in the frequency domain. The rotating transient source terms are projected to high-order degrees of freedom (DOFs) of the finite element problem during their trajectory. They are then transformed to the frequency domain using the Fourier Transform [7]. A Finite Element Method (FEM) mesh is made up of elements that must discretize all of the fuselage's geometrical characteristics. In this case, linear triangular elements with a superficial element size of $3\,\mathrm{mm}$ were used, while tetrahedral

elements were used to fill the volume shown in Figure 2(b). When using linear tetrahedral elements in the propagation volume, the finite element size should be less than $1/6$ of the lowest acoustic wavelength, hence highest frequency, of interest. Because of the adaptive order formulation employed in propagation, this issue can be overcome and coarse volume meshes can be used. The propagation solver automatically changes the order of the element if the mesh discretization is too coarse for the selected frequency. Non-reflective boundary constraints are specified via Automatically Matched Layer (AML) boundaries around the acoustic finite element domain [9]. This enables listeners to be specified outside of the mesh domain. With this approach, it is possible to include the fuselage's scattering effects. Indeed, to validate the acoustic findings against the experimental ones, the fuselage is included in the FEM mesh as well as in the CFD mesh in Section 2.3.

2.3 Free-field sound prediction methodology validation

Intaratep *et al.* [10] measured the Sound Pressure Level (SPL) of a DJI Phantom 2 in hovering conditions. These measurements are used here to validate the quadcopter tonal emissions, as the DJI Phantom 2 uses the same propellers as the Phantom 3 Advanced, and an almost identical fuselage. The spatial position of the microphone used in the experiments to measure the SPL is shown in Figure 3(a). The SPL is expressed in the form:

$$L_p = 10 \log_{10} \frac{p_{\mathrm{rms}^2}}{p_{\mathrm{ref}}^2}, \tag{1}$$

with p_{rms} as the root mean square sound pressure, and $p_{\mathrm{ref}} = 20\,\mu\mathrm{Pa}$ as the reference pressure. The microphone was placed on the $(x, z)(y = 0)$ plane at a distance of $1.51\,\mathrm{m}$ from the quadcopter's center.

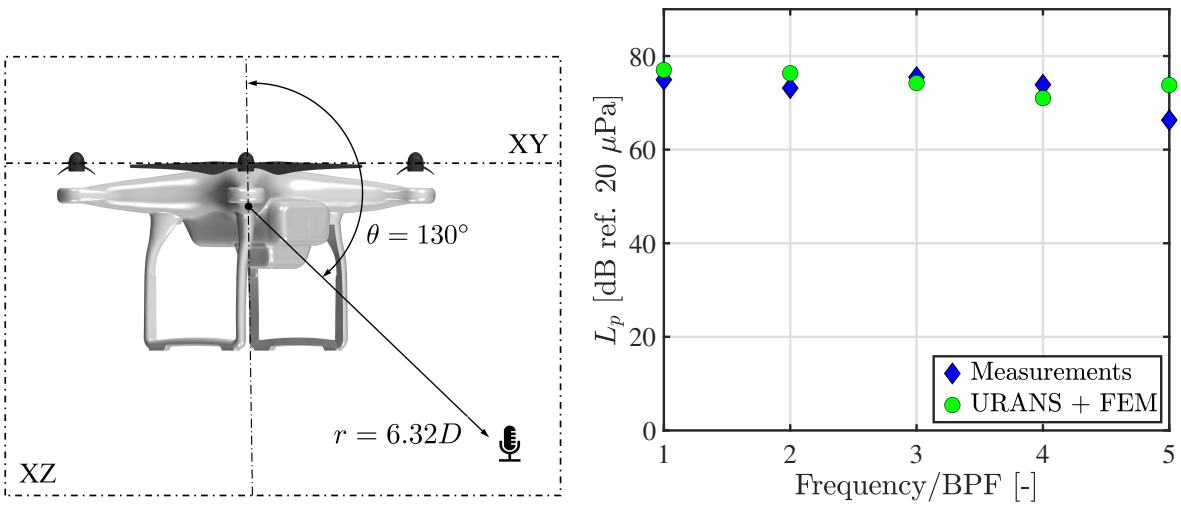

(a) (b)

Figure 3: (a) Microphone position adopted in related reference [10] to measure the quadcopter noise spectrum. (b) Validation of the aeroacoustic prediction methodology against the experimental tonal emission measured in the same reference [10].

When compared to the experimental data, all tones up to the fourth BPF exhibit good agreement as shown in Figure 3(b), with a maximum deviation of $3.5\,\mathrm{dB}$. The described source and propagation methodology will be used in the next sections to propagate the drone noise in urban environments.

2.4 Ray-tracing

Ray-acoustic methods are sometimes referred to as geometrical acoustics. Although, the geometrical surfaces could be either analytical or tessellated, for most realistic engineering cases a triangular tessellation

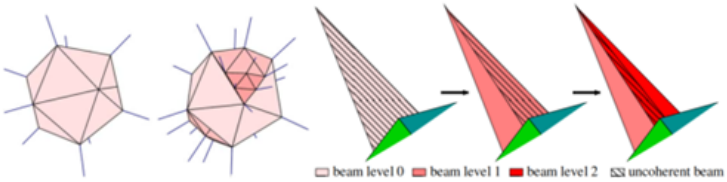

Figure 4: Adaptive Beam Tracing - automatic beam splitting when reflecting on a surface

from a CAD model is used. Unlike the traditional finite elements, the elements' size is governed only by the requirement to accurately capture the geometry yet is not at all related to the frequency range of interest. This also means that there are no extra DOFs and computational costs required to simulate high-frequency acoustics in large environments, which makes it attractive for urban noise footprint simulation. On top of the ability to efficiently compute the acoustic propagation at high frequency, there are three extra requirements on accuracy that the solution should meet:

- Accurately capture reflections on complex curved surfaces.
- Account for the 3D directivity of the source.
- Incorporate the effect of higher-order diffraction.

Below, a very brief description of the Ray Acoustics technology used is described. More elaborate explanations can be found in the related reference [11], for instance.

2.4.1 Ray Acoustics Technology

For this study, Simcenter 3D Ray Acoustics which is based on the ICARE solver from CSTB is used. Ray acoustics technology assumes that sound waves are propagated as rays. This hypothesis is valid at high Helmholtz numbers [12]:

$$He = 2\pi L/\lambda, \tag{2}$$

where L is the characteristic length of the problem geometry and λ is the acoustic wavelength. For typical urban environments, this condition is already met at relatively low frequencies since the scene size is orders of magnitude larger than the wavelength of typical acoustic waves (e.g. 3.4m for a 100Hz acoustic wave). In this section, the main concepts of the ray acoustics technology that are relevant for this application will be discussed.

Adaptive Beam Tracing While simple ray-tracing solutions are based on tracing individual rays launched from a source, the adaptive beam tracing solution used in the context of this paper propagates wave fronts as triangular beams with 3 supporting rays. When these beams reflect on the walls, they are automatically split into smaller beams to keep the coherence between their supporting rays, as illustrated in Figure 4. This way, the solution adapts to the geometry of the problem increasing both the efficiency and accuracy of the calculation.

Smooth Surfaces When working with tessellated convex surfaces, the element normals are typically discontinuous. This leads to a non-physical shadow zone as can be observed in Figure 5. By defining smooth surfaces, the original curvature of the surface is approximated by linear interpolation of the normal. Hence, the solver can accurately model the reflected wave-front, both in terms of ray direction and power decay along its path.

High-order diffraction Beams can also be diffracted. These effects are especially relevant in urban environments where a drone that is hovering around the corner is still audible. Simcenter 3D Ray Acoustics supports multi-order diffraction at sharp edges but also on curved surfaces. This allows capturing creeping waves bending around a curved surface as illustrated in Figure 6.

3D Source Directivity A final important aspect of the realistic acoustic simulation of the drone noise is the ability to incorporate the detailed 3-Dimensional directivity field to characterize the source propagation. This

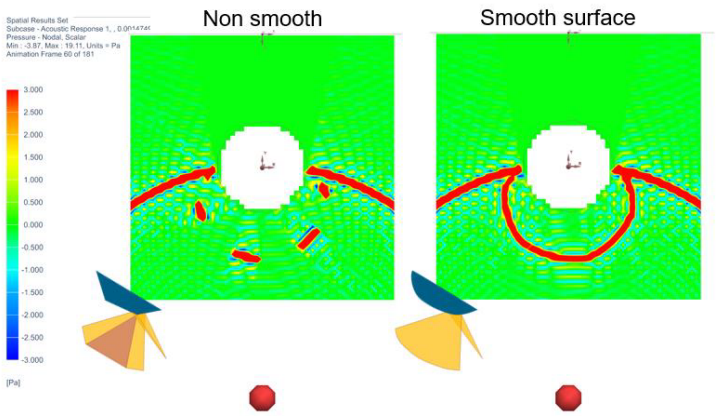

Figure 5: Reflection on a discretized cylinder surface with (right) and without (left) smooth surface correction

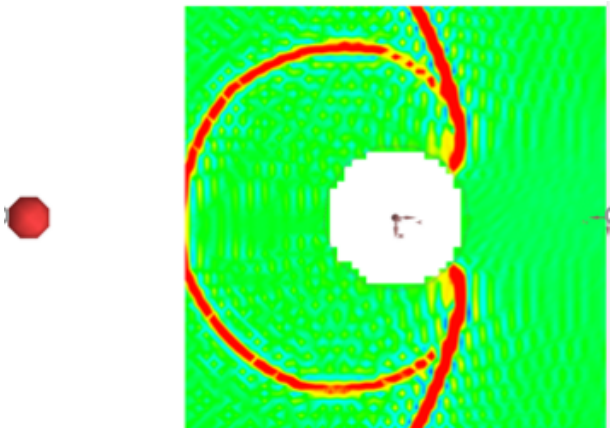

Figure 6: Diffraction of acoustic wave around a discretized cylinder

field is defined as a complex and frequency-dependent factor that scales the source strength radiated in each direction. This directivity field is used to reproduce the equivalent acoustic source strength as evaluated by the free-field FEM model of the drone.

2.5 Source calculation over a sphere

The acoustic field generated by the Finite Element model of the quadcopter is used as input to the Ray Acoustic solution in order to capture the urban footprint. The acoustic pressure radiated from the source is first computed on a spherical microphone mesh surrounding the quadcopter in the Finite Element model. The source is then converted to a point ray source using the directivity information obtained from the first simulation. The rays emitted from the point source assume that both the source strength and the directivity are acoustical quantities which can radiate to far-field. In order to satisfy this, one needs to avoid using source directionality which includes the so-called near-field effects. The radius of the spherical microphone then needs to be large enough to make sure that the far-field conditions are satisfied.

In order to verify this assumption, a set of simulations are run with varying sphere radii for the microphone mesh. The microphone radius was selected as 0.6 and 2.4 wavelengths for the first BPF of the quadcopter. The simulations were run for the first four BPFs of interest. The point source strength with directionality is also scaled with the radius of the microphone selection. Figure 7 shows the four directivity plots for observers located on the rotor plane and 15 wavelengths away from the source. The red line represents the reference results obtained by the Finite Element solution which could radiate the acoustic waves to far-field

without near or far-field assumptions. This is possible since it uses both pressure and its gradient as the source, whereas the ray source uses only the pressure values as input. The thick blue and thin green lines are the results where the directionality is computed around 0.6 and 2.4 wavelengths away from the source for the first BPF, respectively. As seen for the first BPF, the directionality of the close microphones does not converge to the ones from the reference, whereas the microphones located in the far-field provide a better representation of the directionality, since the near-field terms do not contaminate the results. With the increasing BPF, hence decreasing wavelength, the agreement with the closer microphones improves too, as shown in the results for the 4th BPF, for example. However since all the frequencies are captured accurately with it, only the microphones located 2.4 wavelengths away for the first BPF are used in the rest of the simulation.

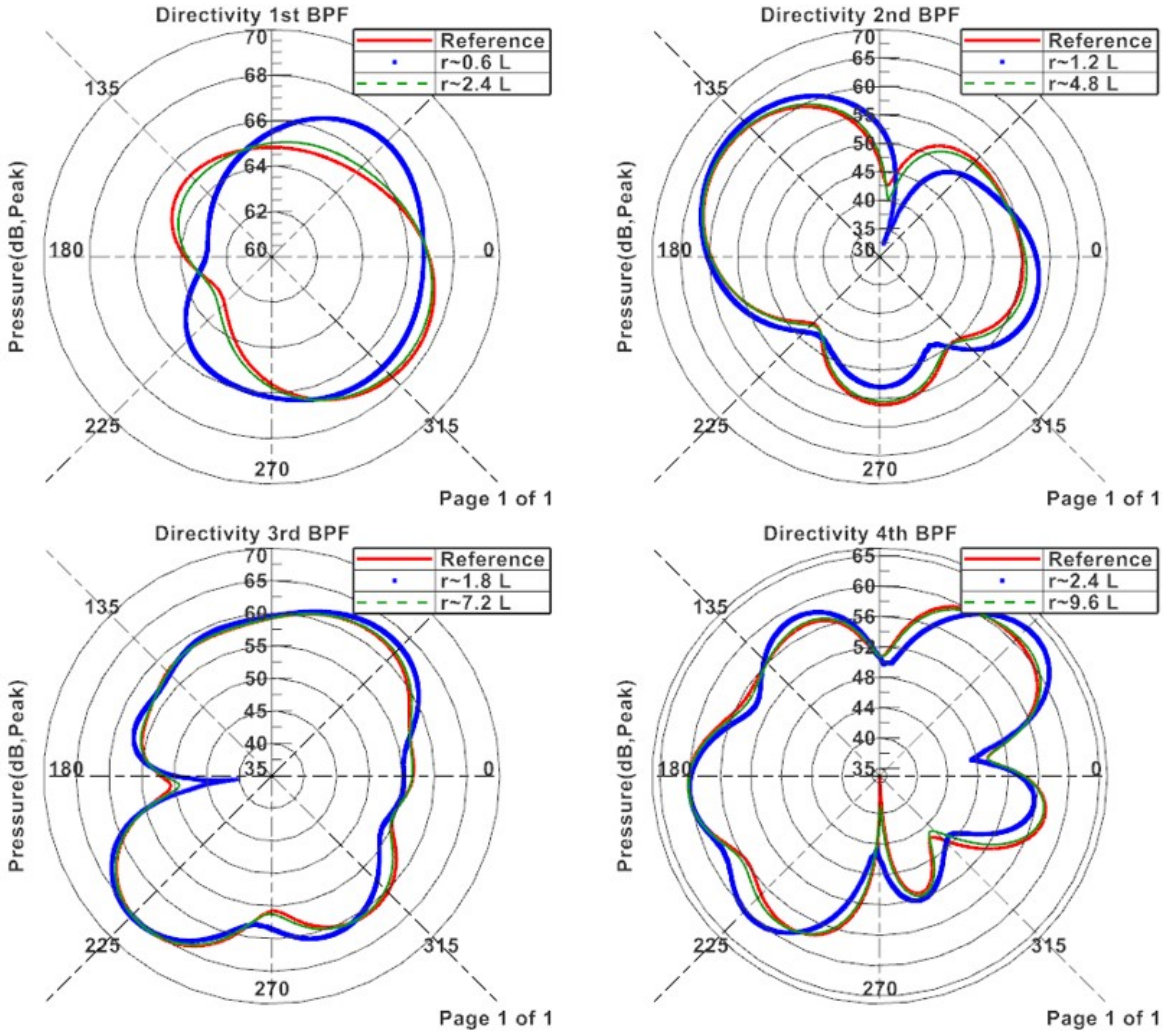

Figure 7: Directivity results comparison with different microphone radii per BPF

3 Results: Urban noise footprint

Once the free-field response is validated and the correct source directionality is obtained, the quadcopter is placed in an urban environment. The Leuven Ladeuzeplein library in Belgium is selected for the computations of the acoustic propagation and reflection effects. The initial sketch of the library and the square which is obtained from the related reference [13] is modified by adding the important reflective surface such as the facade and roof using the commercial software Simcenter 3D [14]. A set of microphones is positioned covering the complete front facade of the library including the windows and the library gallery entrance facing

the square. To avoid numerical singularities arising from overlapping microphone and reflective surfaces on the same location, a 10 cm geometric offset is applied on the microphone plane.

Figure 8 shows the propagated acoustic field from the drone towards the library facade for three drone positions for the first BPF. The quadcopter is positioned around 6 wavelengths away from the library walls and around 3, 6, and 12 wavelengths away from the ground, respectively for the first BPF. The point source location is around the center of the front facade on the horizontal direction. The real part of the acoustic pressure is plotted with the same legends, showing the variation of the acoustic field for different source locations. The rigid reflective ground of the square is also accounted for in the simulations together with the reflections from the rigid library walls including the gallery.

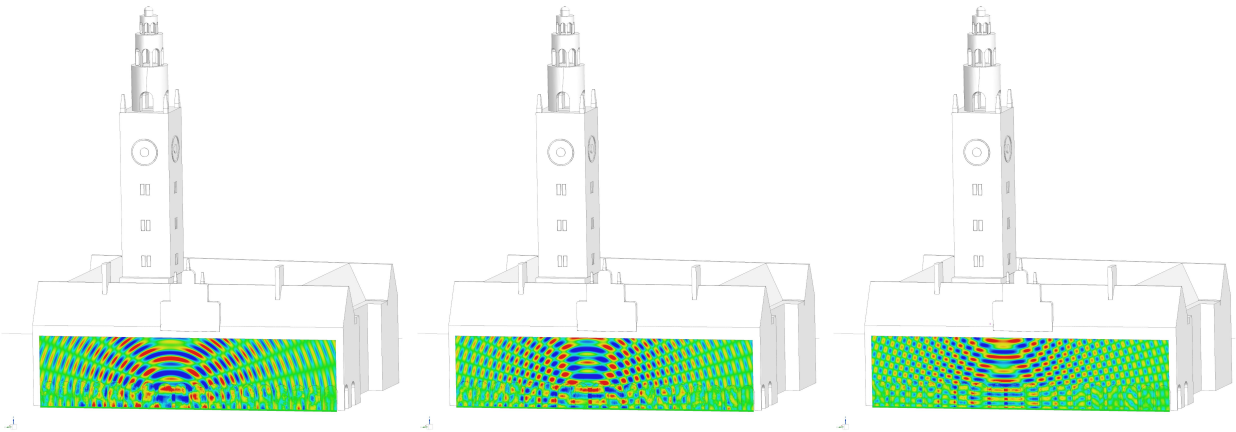

(a) (b) (c)

Figure 8: Acoustic Pressure field at library facade for different hovering positions

To better understand the resulting acoustic field and to capture the different effects of urban components in acoustic propagation, multiple simulations are run with gradually increasing complexity. The drone position is kept as 6 wavelengths away for the first BPF from the library and 12 wavelengths away from the ground.

Figure 9 shows the contour plots of the acoustic pressure for the first and fourth BPFs on the left and right, respectively. A free-field simulation (top) is first run to represent the incident field radiated from the quadcopter. Later, a fully reflective ground is accounted for (center). Finally, the effect of the library walls is added to the ground effects (bottom). The acoustic pressure amplitude is plotted in this qualitative comparison where the interference fringes are clearly visible resulting from the ground reflections. The ground adds up to 3dB to the acoustic field for some of the microphones. Whereas the reflection from the building adds an extra 5dB locally to some of the microphones of interest.

In the bottom row of Figure 9, it is clear that the microphone results facing the library walls are smooth and continuous, whereas the microphones located in the gallery entrance can result in non-smooth patterns. This is due to the extra ray paths computed in the gallery opening of the library. If one wants to neglect these details and assume infinitely long flat walls and ground, analytical representation of these reflections can be accounted for with so-called image sources. The ground can be represented by a mirrored point source. Similarly, the wall can be replaced by another mirrored point source with respect to the facade plane. Finally, one needs to add the fourth point source to account for the cross-reflection. Figure 10 shows the results for the first BPF using reflections from the ground using mirrored point sources (left) and with the ground and an infinitely large facade, using a four-point source configuration (right). It is clear that for the ground reflections, both the Ray solution presented in Figure 9 (c) and image solution shown in Figure 10 (a) converge to the same values since the ground is assumed to be infinitely large in both alternative solutions. This also cross-validates the ray solution for ground reflections.

However, for the facade reflections, one can see that a large part of the microphone results show similarity, as seen in Figure 9 (e) and in Figure 10 (b), except for the reflections around the gallery entrance. This is due to the assumptions made in the image source approach, where the gallery entrance openings are also

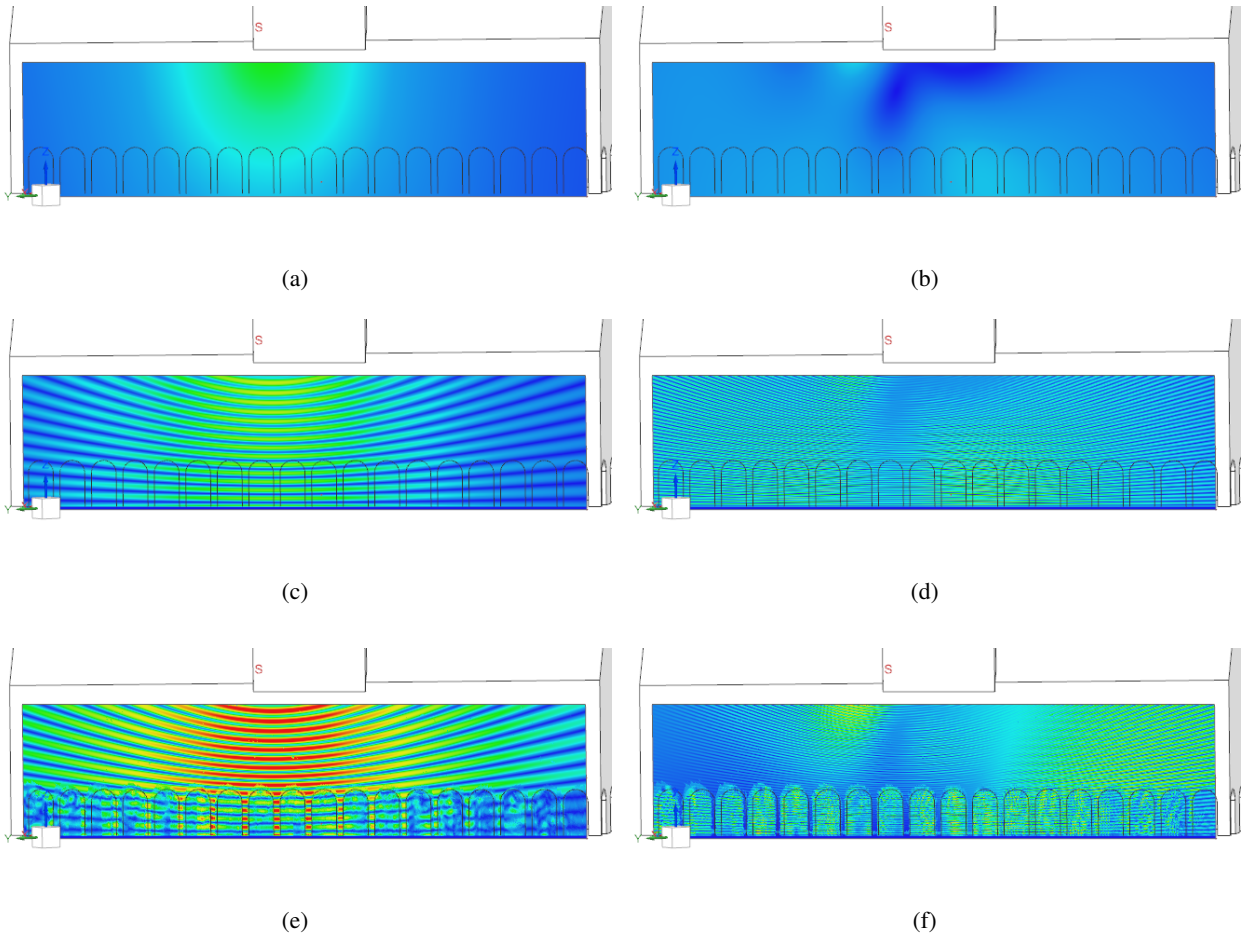

(a) (b)

(c) (d)

(e) (f)

Figure 9: Acoustic Pressure Amplitude at library facade including the reflections computed with ray acoustics

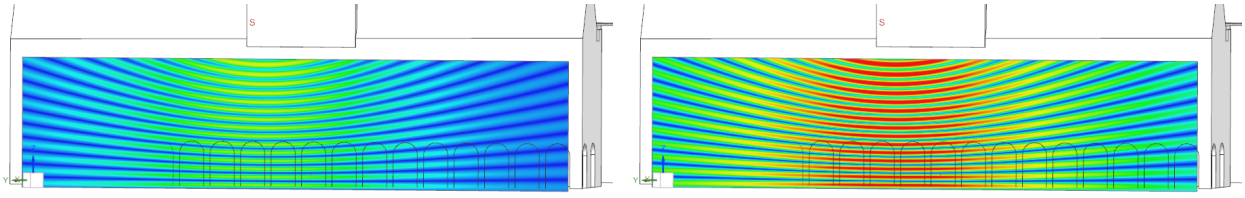

(a) (b)

Figure 10: Reflections with point sources using analytical image sources

represented as rigid walls, which is not the case in reality. In the Ray Acoustics model, on the other hand, the gallery openings and columns are treated properly and not assumed completely rigid.

Therefore, in realistic applications including the actual facade shape which is not infinitely flat due to roof and gallery details, such simplifications no longer hold. This also limits the use of the analytical models and requires the discretization of the model with Finite/Boundary elements, or geometric representation for Ray Tracing. This can even include multiple reflections from various reflective surfaces.

Another aspect of the ray propagation is the computation of the acoustic field, not only with reflections and absorptions, but also with diffraction effects as described in Section 2.4.1. This can be important for the observers which are not located in the direct incident field, or in the direct reflective field. These areas are

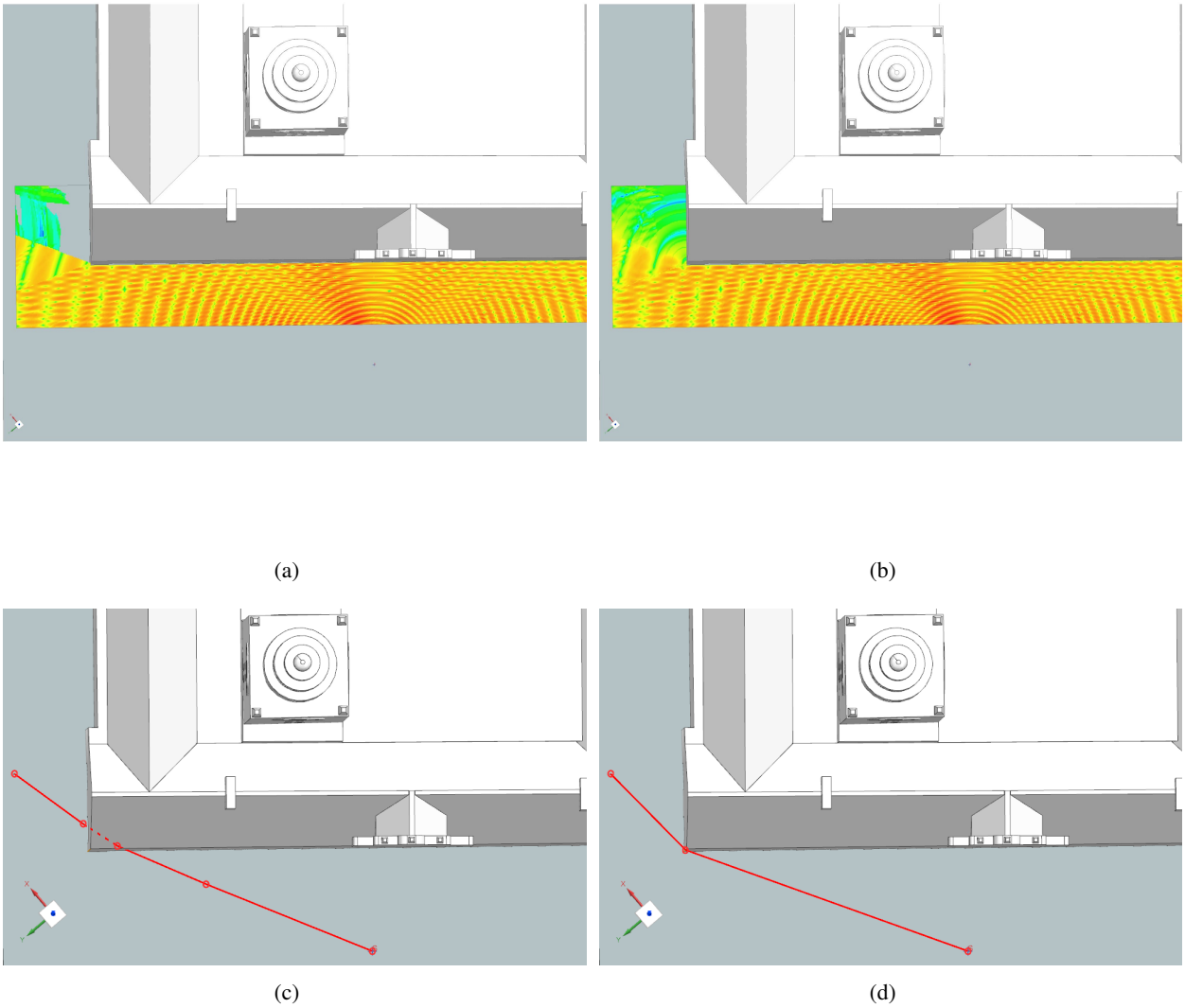

Figure 11: Acoustic Pressure Amplitude without (left) and with (right) diffraction from the edges of the library building

typically referred to as the shadow zone. Figure 11 shows the example of the drone radiation pattern without the diffraction (top left). It is seen that the acoustic field is split into three zones. The first one is the large total field which includes the incident and reflective parts. The second one is the triangle on the left side close to the edge of the building, which includes only the incident field from the source. Finally, the third one is the trapezoidal area which is not receiving either the incident or reflected field from the library walls. There is still some acoustic field received in the shadow zone, which consists of reflected ways from the gallery openings on the front and side of the building. This can be seen in the ray paths plotted (bottom left) where the acoustic fields emitted from the quadcopter are first reflected by the ground (solid red line), then by the floor of the library gallery and reflected the ground back (dashed red lines), and finally received by the observer located on the left top corner of the microphone plane. However, in order to obtain an acoustic field in such shadow areas, diffraction from the edges of reflecting surfaces can be defined. This is shown in Figure 11 (top right) where the same simulation model is computed with extra diffraction defined on the library wall edge. The acoustic field at the shadow zone is still lower than the one of the direct field, however, a more complete acoustic field at the microphones located in side streets is obtained. One of the newly added

ray paths can be seen (bottom right) as the diffraction from the edge of the building. More details on the ray paths will be provided in Section 3.1.

3.1 Ray paths and Echograms

It was shown that the discretization of the facade would include a higher amount of geometrical effects. For example, for someone standing in front of one of the columns of the library entrance, the acoustic field will consist of a direct incident field and reflection from those entities. For high frequencies and lower wavelengths of interest with respect to geometrical details, the incident and reflective field can be tracked.

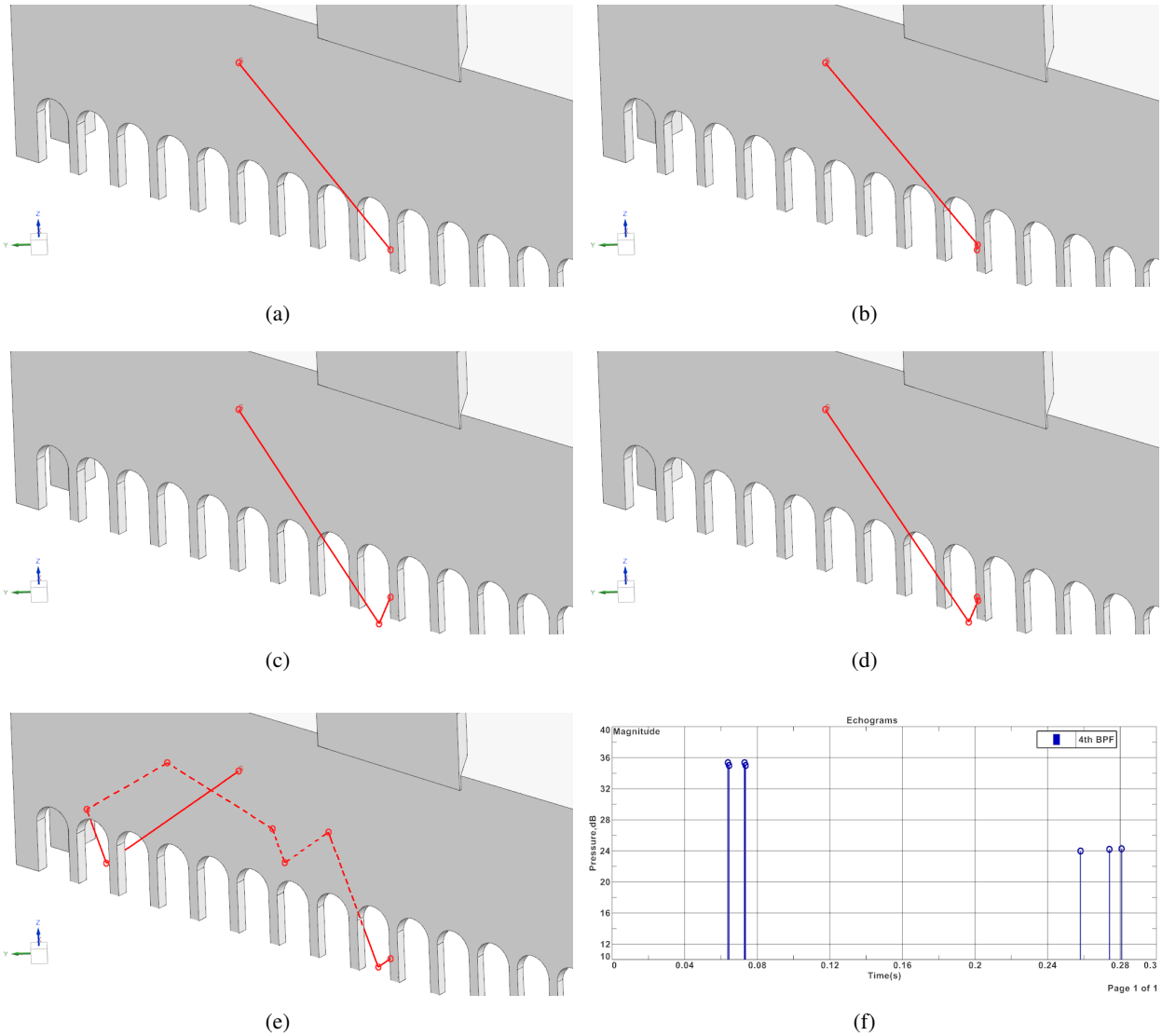

Figure 12: Ray Paths and Echogram in front of the gallery for the 4th BPF

Figure 12 shows the ray paths emitted from the quadcopter located at 6 wavelengths away for the first BPF from the library and 12 wavelengths away from the ground and for an observer located in front of the central columns. The first five ray paths are plotted. The first ray path received by the observer is the direct incident field (top left). The second ray path includes the reflection from the column behind the observer (top right). The third ray path is the one reflected directly from the ground (center left) whereas the fourth ray path is computed as ground reflections reflected once more from the column (center right). For this observer, the fifth ray path is more complex and it includes multiple reflections from the gallery floor and gallery ceiling

(bottom left). The ray paths which are located in the gallery are represented as dashed lines, where the ones out of the building are shown with solid lines.

The arrival times and their contributions are also shown in the echogram in Figure 12 (bottom right). Only the first eight ray paths are shown. As seen in the echogram, the contributions of the first four ray paths are at similar acoustic pressure levels whereas the arrival time of the third and fourth are delayed around 8.5 ms since these paths include ground reflections hence the acoustic rays travel longer. The contribution of the fifth and higher ray paths is lower than the first four. Also, their delay time is around 185 ms due to the complex path that the acoustic rays need to travel.

4 Conclusion

A simulation methodology combining finite volume, finite element, and Ray Acoustics is developed for the noise footprint of a quadcopter hovering in an urban environment. The methodology combines multiple physics and simulation techniques where each component focuses on a simplified part of the problem, hence approaching the multi-scale and multi-physics problem efficiently.

The source field is resolved with URANS and combined with a near-field acoustic propagation code to capture the signature, including the scattering effects of the drone airframe. Using the outcome of these simulation as amplitude and directionality for the considered quadcopter, the complex and large-scale building reflections are taken into account for a ray-based noise propagation solution.

The source and the near-field signature of the drone is validated against experiments. The Ray part is also validated using analytical methods.

The drone is positioned in front of a building and the complex reflection pattern is computed also with different hovering conditions. Also, the complexity of the reflective surfaces increased gradually to see the effects of incident field or reflection from the ground before computing the complete response. The ray paths are computed in order to understand the propagation paths together with an echogram showing the contributions of different paths and their arrival times for the observer.

Compared to free-field propagation, it is shown that reflections should be accounted for a more realistic prediction which is important for the source or observer positions close to the reflective surfaces.

The future work might include accounting for moving sources, such as forward translation, and including atmospheric effects in the larger urban propagation.

Acknowledgements

The authors acknowledge receiving funding from the European Commission's Horizon 2020 research and innovation programme ENODISE under grant agreement number 860103.

References

[1] A. J. Torija and C. Clark, "A psychoacoustic approach to building knowledge about human response to noise of unmanned aerial vehicles," *International Journal of Environmental Research and Public Health*, vol. 18, no. 2, 2021.

[2] A. Zarri, E. Dell'Erba, and C. F. Schram, "Fuselage scattering effects in a hovering quadcopter drone," in *28th AIAA/CEAS Aeroacoustics 2022 Conference*. American Institute of Aeronautics and Astronautics. [Online]. Available: https://arc.aiaa.org/doi/10.2514/6.2022-3031

[3] "Phantom 3 Advanced," https://www.dji.com/be/phantom-3-adv, Accessed: 2022-01-12.

[4] A. Zarri, J. Christophe, S. Moreau, and C. Schram, "Influence of Swept Blades on Low-Order Acoustic Prediction for Axial Fans," *Acoustics*, vol. 2, no. 4, pp. 812–832, Nov. 2020. [Online]. Available: https://www.mdpi.com/2624-599X/2/4/46

[5] F. R. Menter, "Two-equation eddy-viscosity turbulence models for engineering applications," *AIAA Journal*, vol. 32, pp. 1598–1605, 1994.

[6] C. Russell, J. Jung, G. Willink, and B. Glasner, "Wind tunnel and hover performance test results for multicopter UAS vehicle," in *AHS* 72^{nd} *Annual Forum*, West Palm Beach, FL, USA, May 2016.

[7] *Simcenter Nastran Acoustics User's Guide (version 2022.1)*, Siemens, 2022.

[8] M. Roger, *Aeroacoustics of installed propellers*, ser. von Karman Institute Lecture Series. von Karman Institute for Fluid Dynamics, 2019, no. 2019-02.

[9] H. Bériot and A. Modave, "An automatic perfectly matched layer for acoustic finite element simulations in convex domains of general shape," *International Journal for Numerical Methods in Engineering*, vol. 122, no. 5, pp. 1239–1261, 2021.

[10] N. Intaratep, W. N. Alexander, W. J. Devenport, S. M. Grace, and A. Dropkin, "Experimental Study of Quadcopter Acoustics and Performance at Static Thrust Conditions," in *22nd AIAA/CEAS Aeroacoustics Conference*. Lyon, France: American Institute of Aeronautics and Astronautics, May 2016. [Online]. Available: https://arc.aiaa.org/doi/10.2514/6.2016-2873

[11] N. Noe, C. Rougier, J. Rouch, and I. Schmich, "An hybrid beam and particle tracing with time dependant radiosity for accurate impulse response of rooms prediction," in *Acosutics 2012*, Nantes, France, 2012.

[12] A. Atkins, T. Atkins, and M. Escudier, *A dictionary of mechanical engineering*. Oxford University Press, 2013.

[13] "Cadmapper," https://cadmapper.com/, Accessed: 2022-05-01.

[14] "Simcenter 3D," https://support.sw.siemens.com/, Accessed: 2022-06-01.